Direct numerical simulation of a freely decaying turbulent interfacial flow

P. Trontin [a,*], S. Vincent [b], J.L. Estivalezes [a], J.P. Caltagirone [b]

[a] ONERA/DMAE, 2, avn Edouard Belin, 31055 Toulouse, France
[b] Université Bordeaux I, TREFLE-ENSCPB, UMR 8508, 16, avn Pey-Berland, 33607 Pessac Cedex, France

ARTICLE INFO

ABSTRACT

Whereas Large Eddy Simulation (LES) of single-phase flows is already widely used in the CFD world, even for industrial applications, LES of two-phase interfacial flows, i.e. two-phase flows where an interface separates liquid and gas phases, still remains a challenging task. The main issue is the development of subgrid scale models well suited for two-phase interfacial flows. The aim of this work is to generate a detailed data base from direct numerical simulation (DNS) of two-phase interfacial flows in order to clearly understand interactions between small turbulent scales and the interface separating the two phases. This work is a first contribution in the study of the interface/turbulence interaction in the configuration where the interface is widely deformed and where both phases are resolved by DNS. To do this, the interaction between an initially plane interface and a freely decaying homogeneous isotropic turbulence (HIT) is studied. The densities and viscosities are the same for both phases in order to focus on the effect of the surface tension coefficient. Comparisons with existing theories built on wall-bounded or free-surface turbulence are carried out. To understand energy transfers between the interfacial energy and the turbulent one, PDFs of the droplet sizes distribution are calculated. An energy budget is carried out and turbulent statistics are performed including the distance to the interface as a parameter. A spectral analysis is achieved to highlight the energy transfer between turbulent scales of different sizes. The originality of this work is the study of the interface/turbulence interactions in the case of a widely deformed interface evolving in a turbulent flow.

1. Introduction

Direct numerical simulations (DNS) of interface/turbulence interaction are relatively recent (Lam and Banerjee, 1988; Lam and Banerjee, 1992) and generally limited to plane free-surface configurations where the effect of the gas phase on the liquid is neglected and replaced by the free plane surface approximation sometimes in combination with an enforced shear force. Free surface turbulence in an open channel flow was first studied by Lam and Banerjee (1988), Lam and Banerjee (1992). Lombardi et al. (1996) performed a DNS of counter-current gas–liquid flow in a channel using free-slip boundary conditions at both channel walls. The interface between the two phases was maintained flat which corresponds to a very high surface tension. It was found that turbulence characteristics on the gas side are similar to those at the near wall, and that the lighter phase might seem like a solid surface at the interface. Later, Handler et al. (1993) conducted similar DNS In these simulations, the free surface was supposed to be a rigid free-slip wall and the vertical movement of the free surface was ne-

glected. The full free surface boundary conditions were integrated in the work of Komori et al. (1993). But this work was still restricted to small-amplitude surface deformations. A model of wind-generated surface waves was proposed by Borue et al. (1995) by studying the influence of enforced stresses at the free surface. Non-flat interfaces were investigated by De Angelis (1998) by considering stratified flows with a freely deformable interface in the capillary wave regime. Fulgosi et al. (2003) performed DNS of turbulence in a counter-current air–water flow configuration separated by a deformable interface. The results of this work did not differ very much from the previous investigation (Lombardi et al., 1996). Turbulence intensities, budgets for the Reynolds stresses and flow structures on the gas side showed similarities with results issued from an open channel flow. In Banerjee et al. (2004), friction velocities were considerably increased so as to generate surface deformations of higher waveslopes, without leading to wave breaking. It was found (Banerjee et al., 2004) that when the shear rate imposed by the gas is high, turbulence is generated in the vicinity of the interface, like near solid boundaries. In Lakehal et al. (2005), the DNS of the stratified gas–liquid flow over a sheared interface concluded in the necessity to accomodate the asymptotic behaviour of turbulence near interfaces (like in wall flows). The first damping function for near-interface turbulence from the gas side was derived (Lakehal et al., 2005). In all these studies, the interface

---

* Corresponding author. Present address: ONERA/DSNA - BP 72, 29, avn de la Division Leclerc, 92322 Châtillon Cedex, France.
E-mail address: pierre.trontin@onera.fr (P. Trontin).

deformation is supposed to be moderated excluding strong topological changes such as fragmentation or wave breaking.

More recently, work has been done taking into account fragmentation or break-up in the DNS context of two-phase separated flows. Indeed, Bunner and Tryggvason (2003) have studied the effect of bubble deformation on the properties of turbulent bubbly flows. In their simulations, turbulence was produced by the wake of bubbles. The so-called pseudo-turbulence induced by a bubble swarm does not have the same properties as a well developed turbulence whose energy spectrum contains an inertial zone. Few DNS studies of deformable bubbles have been carried out in turbulent channel flows. Among them, in Kawamura and Kodama (2002), DNS of a fully developed turbulent channel flow containing deformed bubbles are performed. A front-tracking method is used to capture the interface. Modifications in the profiles of turbulence intensities were observed. In Liovic and Lakehal (2007a) a LES formulation has been applied to a turbulent bubbling process driven by a constant volume injection of air into a water pool. A strong correlation between turbulence and interface deformations was found. In more recent works, Toutant et al. (2007) investigated by DNS the motion of a strongly deformable bubble without ruptures in a spatially decaying turbulence in order to perform *a priori* filtering for LES modelling of interfacial two-phase flows. Liovic and Lakehal (2007b) develop a new strategy around the LES simulation of interfacial flows based on a multi-physics treatment in the vicinity of deformable gas–liquid interfaces. A reconstructed distance function is introduced, on which an interfacial shear velocity is defined to be used in near-interface transport models. This methodology (Liovic and Lakehal, 2007b) has been applied for the simulation of a wave breaking configuration.

The aim of the work presented in this paper is the study of the evolution of an interface separating two immiscible fluids in a free decaying turbulence. The interface appears to be widely deformed. Both liquid and gas phases will be resolved with DNS and turbulent statistics will be carried out on both phases as well as a detailed spectrum analysis. In order to focus on interface–turbulence interactions, it was decided to work with the same density and dynamic viscosity for both fluids. This work is a first contribution in the study of the interaction between an interface and turbulence when the interface is widely deformed. Because of the complexity in the topology of the interface (the aim is to mimic atomization process), quantitative analysis is less obvious. This work is a first step in the understanding of interface/turbulence interactions in complex situations (typically atomization) and not a global and exhaustive study of interfacial multiphase flows.

In a first part governing equations are introduced. In a second part numerical methods are presented. Then, in a third part, the numerical simulations are analyzed. This part is divided into two sections. The first one is about the single-phase simulation and the validation of the DNS of the homogeneous isotropic turbulence (HIT) flow. The second section is dedicated to the HIT flow in which a sheet has been added. After having presented the numerical configuration, the interface/turbulence mechanism is studied. Then 3D energy spectra are performed and finally 2D energy spectra are studied in planes parallel to the initial sheet.

2. Governing equations

The simulation of liquid–gas flows at moderate velocities is under consideration assuming an isothermal behaviour. The incompressible Navier–Stokes equations are used to model the resulting two phase flow (Scardovelli and Zaleski, 1999)

$$\rho(\mathbf{u}_t + (\mathbf{u} \cdot \nabla)\mathbf{u}) = -\nabla p + \nabla \cdot \mathbf{D}$$
$$\nabla \cdot \mathbf{u} = 0 \tag{1}$$

where ρ is the density, p the pressure, $\mathbf{u}$ the velocity vector, $\mathbf{D} = \mu(\nabla\mathbf{u} + \nabla^T\mathbf{u})$ the viscous stress tensor for a Newtonian fluid and μ the dynamic viscosity. The boundary conditions at the interface between two immiscible fluids are the continuity of the velocity components

$$[\mathbf{u}]_\Gamma = 0 \tag{2}$$

and the dynamic boundary conditions for the normal and tangential stresses (Delhaye, 1974)

$$[p]_\Gamma - \mathbf{n} \cdot [\mu\mathbf{D}]_\Gamma \cdot \mathbf{n} = \sigma\kappa \tag{3a}$$
$$\mathbf{t} \cdot [\mu\mathbf{D}]_\Gamma \cdot \mathbf{n} = 0 \tag{3b}$$

where $\mathbf{n}$ and $\mathbf{t}$ are respectively the normal and the tangent vectors to the interface. σ is the surface tension coefficient and κ the local curvature of the interface. The brackets $[\mathbf{u}]_\Gamma$ for example stand for the velocity jump across the interface.

3. Numerical methods

3.1. Navier–Stokes solver

Classical projection methods are performed to ensure the incompressibility constraint (Chorin, 1968; Temam, 1969). The spatial discretization is based on staggered MAC (Harlow and Welsh, 1995) uniform Cartesian grids for the velocity components, all others quantities as density, pressure and level-set are cell-centered. The convection terms in the momentum equations are approximated in a conservative way with 5th order accurate WENO schemes (Shu, 1997). This particular choice has been motivated by the robustness and low numerical dissipation of such schemes to perform direct numerical simulations (Trontin et al., 2008). Time integration is performed with a 3rd order accurate TVD Runge–Kutta scheme. It should be pointed that the incompressibility constraint is enforced at each Runge–Kutta sub-step. The Poisson equation for the pressure is solved by a fast multigrid preconditioned conjugate gradient method (Tatebe, 1996; Trottenberg and Schuller, 2001).

3.2. Interface-capturing method

A level-set method (Osher and Sethian, 1988; Sussman et al., 1994) is used to capture the interface, which is implicitly given by the zero of the smooth function $\phi(\mathbf{x},t)$. By convention, the level-set function ϕ will be taken positive in the liquid and negative in the gas and the normal $\mathbf{n}$ will point towards the positive values of ϕ. Moreover, ϕ is imposed to be the signed distance function to the interface. This particular property of the level-set function is of major importance. Indeed, this property ensures the level-set to be well behaved at the interface between the two fluids. The evolution of the interface is implicitly captured by the zero-level of ϕ which obeys the following equation

$$\phi_t + (\mathbf{u} \cdot \nabla)\phi = 0 \tag{4}$$

As for the momentum equation, the level-set equation is solved by a 5th order conservative WENO scheme for spatial discretization and a 3rd order TVD Runge–Kutta scheme. While Eq. (4) will move the level-set $\phi = 0$ at the correct velocity, ϕ will no longer remain a distance function ($|\nabla\phi| \neq 1$). This can lead to large mass losses or gains as the interface will behave poorly. Consequently, the level-set must be regularly reinitialized to overcome this drawback. This is achieved by solving to the steady state the following Hamilton–Jacobi equation for ϕ (Sussman et al., 1994; Jiang and Peng, 2000)

$$\phi_t = S(\phi_0)\left(1 - \sqrt{\phi_x^2 + \phi_y^2}\right)$$
$$\phi(x,y,0) = \phi_0(x,y) \tag{5}$$

Eq. (5) has the property that ϕ remains unchanged at the interface, then the zero of the level-set ϕ_0 and ϕ are the same and the steady state solution of (5) verifies $|\nabla \phi| = 1$. The Eq. (5) is solved by a Godunov type scheme with a fifth order WENO scheme. As a distance level-set is sought only in the vicinity of the interface, few pseudo time steps are needed to reach a distance level-set again.

3.3. Ghost fluid approach for the jump conditions

The jump conditions for pressure and pressure gradient in the Poisson pressure equation as well as jump condition for the viscous terms are taken into account by the ghost fluid method (Fedkiw et al., 2000). The full mathematical details of this method can be found in Couderc (2007). The authors have validated the numerical methods in Trontin et al. (2008).

4. Numerical simulation

To understand the interaction between small scales of turbulence and an interface, the classical configuration of homogeneous isotropic turbulence (HIT) is chosen. In any direct numerical simulation of turbulent flows, adequate resolution of the smallest spatial scales is of primary importance. Here, different length scales as well as statistical parameters are calculated to assess the reliability of the simulation.

4.1. Homogeneous isotropic turbulence simulation: single-phase case

The computational domain is a 2π square box with periodic boundary conditions on each side. The spatial grid resolution is 512^3. The time step corresponds to $\frac{1}{50}$ of the Kolmogorov time scale. Simulations are performed at low Reynolds numbers. Parameters given by Mansour and Wray (1994) are chosen to initiate the HIT field. This field is generated in Fourier space: it fulfills the constraint of incompressibility and follows a prescribed energy spectrum. A complete description of the method to initiate an HIT field can be found in Rogallo (1981). The initial energy spectral density (energy spectrum) is given by

$$E(k) = \frac{r^2}{2A} \frac{1}{k_p^{\gamma+1}} k^\gamma \exp\left(-\frac{\gamma}{2} \left(\frac{k}{k_p} \right)^2 \right) \qquad (6)$$

where k_p is the wave number for which $E(k)$ is maximum, γ and r are parameters, and

$$A = \int_0^\infty k^\gamma \exp(-\gamma k^2/2)\, dk$$

Here, $r^2 = 3$, $\gamma = 4$ and $k_p = 9$. All the parameters of the calculation are summarized in Table 1. The turbulent kinetic energy (herein after TKE) q

$$q = \frac{1}{N^3} \sum_{i,j,k} 0.5(u_{i,j,k}'^2 + v_{i,j,k}'^2 + w_{i,j,k}'^2)$$

is defined as the half trace of the Reynolds stress tensor. The turbulent velocity scale is then defined by $u' \equiv \sqrt{\overline{u'^2}} = \sqrt{\frac{2}{3}q}$. The statistical averaging $\overline{}$ is approximated here by volume averaging. Time evolution of TKE q is represented in Fig. 1. Comparisons are carried out between our 512^3 DNS code and a 128^3 DNS spectral code. It can be seen that 512^3 resolution gives the same accuracy than 128^3

Table 1
Parameters of the initial turbulence.

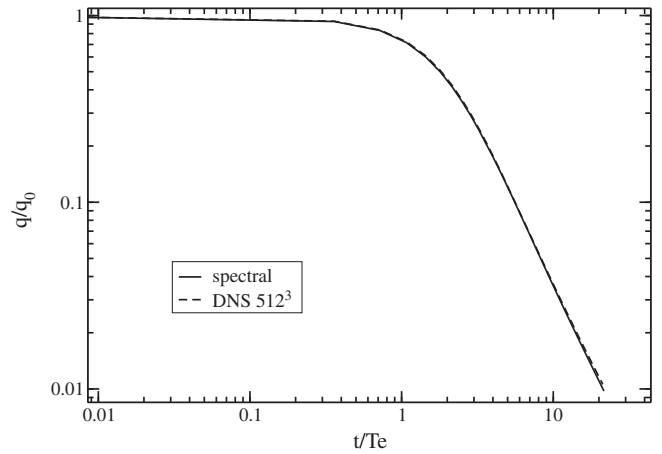| v	u'	ϵ	L_f	λ	η_k	T_e	R_{L_f}	R_λ
0.003	1.0	0.911	0.279	0.222	1.312×10^{-2}	0.278	93	74

Fig. 1. Time evolution of turbulent kinetic energy.

spectral DNS (which is already well resolved). It can be concluded that the 512^3 simulation is a DNS. In Fig. 2 the normalized TKE dissipation rate ϵ increases at early stages from $\frac{t}{T_e} = 0$ to 1. T_e is the Eulerian time scale or eddy turnover time based on large scales of turbulence. As observed by Yu et al. (2005), this increase of $\frac{\epsilon}{\epsilon_0}$ is consistent with known turbulence physics: at early stages the energy spreads to higher wave numbers due to the nonlinear cascade process. This phenomenon leads to the increase of the dissipation rate in physical space, as shown in Fig. 2. For later times (after one eddy turnover time here), the dissipation decays monotonically. Once again, a comparison between our 512^3 DNS code and a 128^3 DNS spectral code is performed showing an accuracy of the 512^3 DNS comparable to the spectral simulation. In Fig. 2, the budget $\epsilon = -\frac{dq}{dt}$ is satisfied indicating the good resolution of the computation. In Fig. 3, the ratio $\frac{d\epsilon}{dt} / \left(\frac{\epsilon^2}{q} \right)$ is plotted and is -1.57. In the case of large Reynolds numbers simulation, this constant is supposed to be -1.96. The difference is due to our direct simulations where Reynolds numbers are moderate. Higher order moments can be calculated to measure the turbulence evolution from $t = 0$. Skewness and flatness factors (Pope (2000)) are represented in Fig. 4. They respectively represent 3th and 4th order moments of spatial derivatives of u'. S and F measure the gap between the calculated spatial derivatives of u' and a Gaussian repartition of these derivatives. S and F are given by

$$S = \frac{1}{3} \overline{\left(\frac{\partial u_i}{\partial x_i} \right)^3} \bigg/ \overline{\left(\frac{\partial u_i}{\partial x_i} \right)^2}^{3/2}$$
$$F = \frac{1}{3} \overline{\left(\frac{\partial u_i}{\partial x_i} \right)^4} \bigg/ \overline{\left(\frac{\partial u_i}{\partial x_i} \right)^2}^{2} \qquad (7)$$

Several experimental studies (Mills et al., 1958; Smith and Reynolds, 1992) have shown that

$$-0.5 \leqslant S \leqslant -0.4$$
$$3.3 \leqslant F \leqslant 4 \qquad (8)$$

when turbulence is fully established. In this work, Fig. 4 shows that after three eddy turnover times, the turbulence can be considered as fully established. If R_λ is referred to as the Reynolds number based on λ, the Taylor micro-scale, Mansour and Wray (1994) have shown that the skewness factor collapses for very small R_λ (about 5 for this configuration). To avoid this collapse, numerical simulations are stopped in the rest of the work at a final time which ensures that $R_\lambda \geqslant 10$.

Concerning the DNS spatial resolution, good resolution of the smallest scales is needed to avoid energy pile-up at high wave
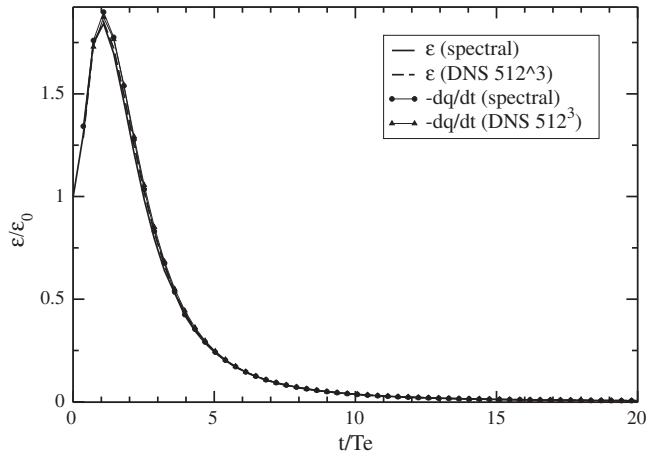
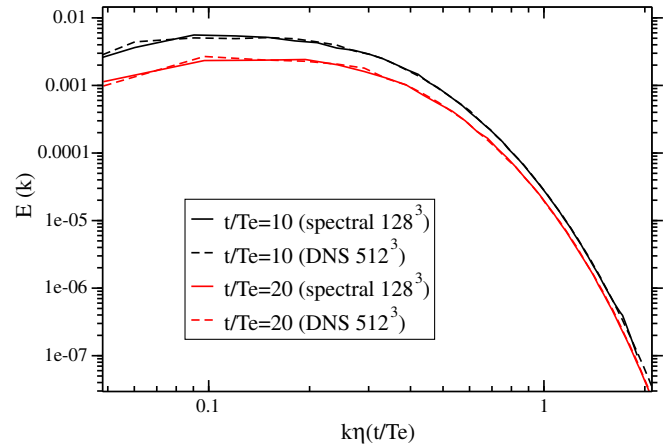**Fig. 2.** Time evolution of turbulent kinetic energy dissipation rate.

Fig. 5. 3D energy spectra at two different $\frac{t}{T_e}$. Comparison between 128^3 spectral code and 512^3 DNS.
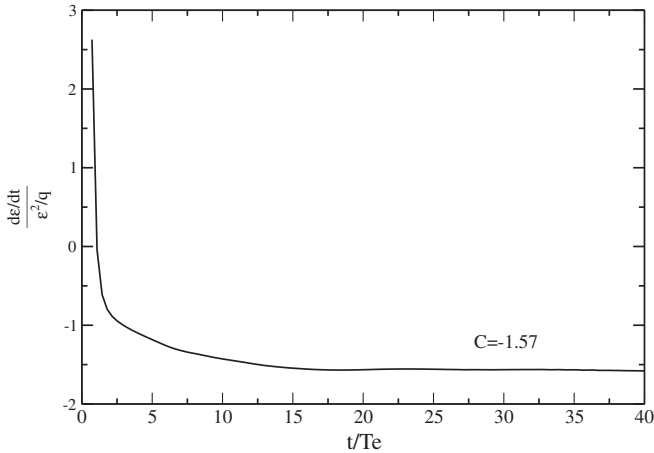

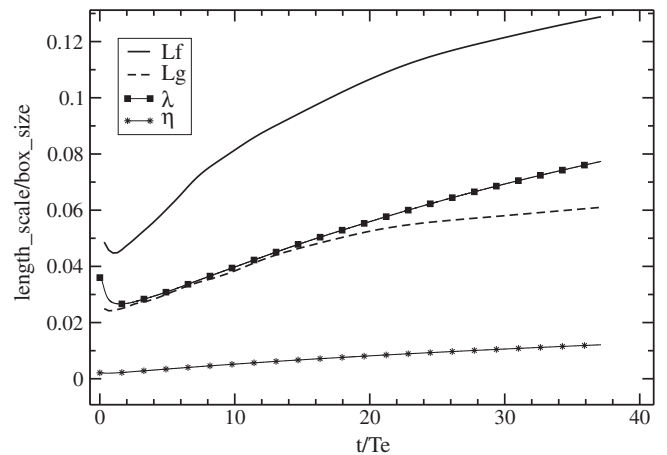**Fig. 3.** $q - \epsilon$ model for turbulence. Plot of the ratio $\frac{\frac{\partial \epsilon}{\partial t}}{\epsilon^2/q}$.

Fig. 6. Time evolution of turbulent length scales.
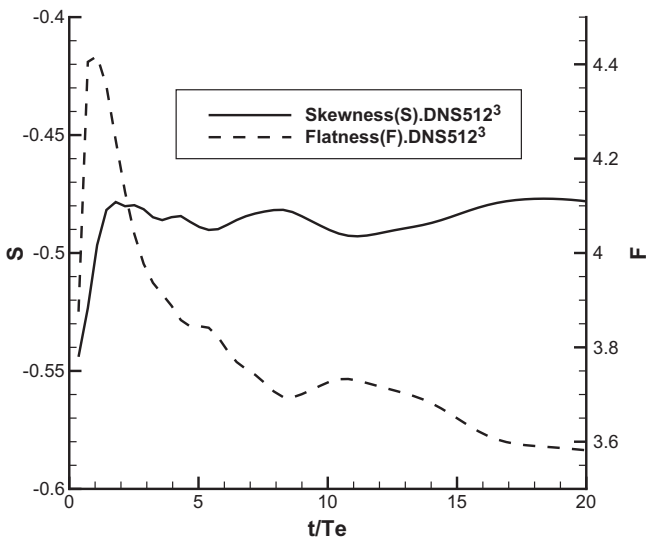
Fig. 4. Skewness and flatness numbers vs. t/T_e.

numbers. Theoretically, the numerical cut-off wave number is given by $k_{\max}\eta_k = \pi(\frac{\eta_k}{\Delta x} = 1)$, where η_k is the Kolmogorov length scale, $k_{\max}$ is the highest simulated wave number and Δx is the grid

size. However, $k_{\max}\eta_k \simeq 1.5$ is generally used as a necessary condition for DNS resolution (Yeung and Pope, 1988). It could be shown that $k_{\max} \eta_k > \pi$ with 512^3 grid points for initial conditions given by (6). In Fig. 5, 3D energy spectra are plotted for two different times. Comparisons are made between the 128^3 spectral code and our 512^3 DNS code. Every turbulent scale is accurately captured by the 512^3 DNS, even for the smallest scales (high wave numbers), showing 512^3 resolution is accurate enough for this simulation.

Fig. 6 shows the time evolution of the turbulence length scales. Every length scale increases in time. At the end of the simulation $\frac{L_b}{L_f} = 7$, where L_b and L_f are respectively the box size and the Eulerian longitudinal integral length scale. According to Boughanem and Trouvé (1996), $\frac{L_b}{L_f} \geqslant 8$ is needed to ensure the decorrelation of the velocity field with the box length scale. Such a condition is respected for $\frac{t}{T_e} \leqslant 32$ as shown in Fig. 6. In this figure, the Howarth and Karman relation (Howarth and Karman, 1938) between L_f and L_g is well observed $\left(\frac{L_f}{L_g} = 2\right)$ where L_g is the Eulerian transversal integral length scale.

4.2. Sheet in a HIT flow: interface–turbulence interaction

4.2.1. Configuration

As shown in Fig. 7, a thin plane layer (or sheet hereafter) is added in the HIT field generated from the energy spectrum given by Eq. (6). The sheet is represented by the fluid 2 in Fig. 7. Its
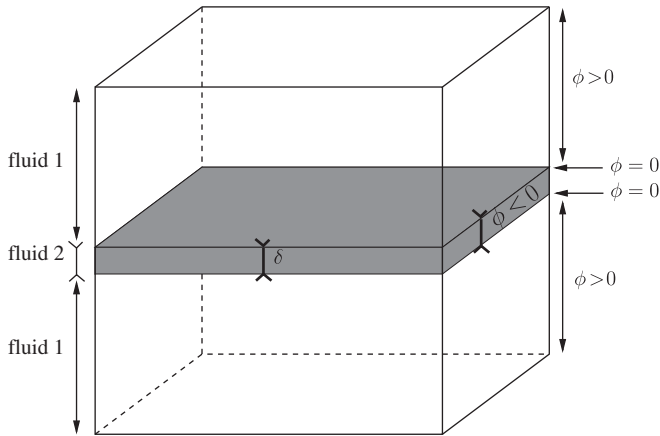
Fig. 7. Layer (or sheet) in a HIT flow: initial configuration. Periodic boundary conditions are enforced in the three directions. Fluid 1 is represented by $\phi > 0$ and fluid 2 by $\phi < 0$. At $t = 0$, the two fluids 1 and 2 are separated by two planar interfaces $\phi = 0$.

thickness δ is 5 % of the box size and compared to the Kolmogorov spatial scale, $\frac{\delta}{\eta_k} = 24$. The sheet is the set of points $\mathbf{x}$ such as $\phi(\mathbf{x}) < 0$. Up and down the sheet, the fluid 1 is characterized by the set of points $\mathbf{x}$ such as $\phi(\mathbf{x}) > 0$. The iso-surface $\phi = 0$ is the interface between the two fluids. Periodic boundary conditions are enforced on the whole computational domain. Therefore, the initial configuration is a thin plane layer or sheet (such as $\phi(\mathbf{x}) < 0$, i.e. fluid 2) inside the fluid 1 (such as $\phi(\mathbf{x} > 0$). Turbulence is generated is the whole computational domain, both in the fluid 1 and in the fluid 2. Initially plane, the sheet follows the motion of the surrounding turbulent flow. The aim of this work is the study of the interaction between turbulence and capillary forces without any other influence such as gravity forces or other volumic forces. Indeed, the results presented here will be used to perform *a priori* filtering for LES simulation of air-blasted atomization where gravity could be completely neglected. Moreover, viscous and density jumps are not taken into account, so that $\frac{\rho(\phi<0)}{\rho(\phi>0)} = 1$ and $\frac{\mu(\phi<0)}{\mu(\phi>0)} = 1$. A parametric study is performed on the surface tension coefficient σ. The dimensionless relevant number is the Weber number comparing the fluid inertia to its surface tension force. It is given by $W_e = \frac{\rho u_0'^2 \delta}{\sigma}$, where $u_0' \equiv \sqrt{\overline{u'^2(t)}}_{t=0}$ is the initial turbulent velocity and δ is the thickness of the sheet. The sheet in the HIT field was studied for different W_e values: 110, 63, 19, 2 and 0.2. The reference case is the HIT flow with no interface. It is equivalent to a sheet where $\sigma = 0$. In this configuration, the sheet just behaves like a Lagrangian marker. That is why the reference case will be referred to as $W_e = \infty$.

4.2.2. Interaction mechanism and turbulent statistics
4.2.2.1. Qualitative overview.
We first consider the interaction mechanism with respect to the topological changes of the interface between the two phases. They are represented in Fig. 8 for four different initial W_e and at three different times. For high W_e numbers (small surface tension forces) the interface is widely stretched by the surrounding turbulence. Filaments and small structures appear. When time increases, these structures become bigger and their shapes tend to be spherical. This is due to capillary forces which become more important as time increases. Indeed, as local curvatures of the sheet increase (compared to the initial flat configuration of the interface), surface tension forces increase as well. For the lowest W_e number (high surface tension forces), however, the initial planar sheet is only slightly disturbed. In this case, no tearing or stretching of the interface is observed. It could be thought that the interface behaves as a solid wall. From these qualitative

results, it can be shown that highest Weber numbers produce small droplets, which is consistent with earlier formation of very thin ligaments whereas lowest ones keep the sheet nearly plane, indicating some critical Weber number under which no fragmentation occurs. This critical Weber numbers lies between 0.2 and 2.

4.2.2.2. PDF of droplets distribution.
As the interface topology of the highest Weber numbers is finely grained, one could ask if the simulation is real DNS with respect to the interface. To deal with, in Figs. 9–11, the PDFs of the number of droplets vs. $D/\Delta x$ are plotted for three different W_e numbers at different times, where D is the diameter of the droplet and Δx the spatial step. Practically, this diameter is calculated by $D = \left(\frac{6V}{\pi}\right)^{1/3}$, where V is the volume of each blob detected by a geodesic reconstruction algorithm (Serra, 1983). In Figs. 9–11, a zoom is performed for $50 \leqslant D/\Delta x \leqslant 250$ and the result is shown in the right up corner of the figure. For early times ($t/T_e \leqslant 5$) and for $W_e = 110$ and $W_e = 19$ (Figs. 9 and 10), the PDFs show a maximum for $1 \leqslant D/\Delta x \leqslant 20$, indicating a strong fragmentation of the sheet due to ligament break-up. However, as described in the zoom of Figs. 9 and 10, the single path-connected component of the sheet is still present for this time. Its equivalent diameter decreases from 234 to 230 for $W_e = 110$ and from 234 to 220 for $W_e = 19$. For later times, coalescence happens as shown in Figs. 9 and 10. For these Weber numbers, the largest number of droplets is observed for $D/\Delta x = 10$ at $t/T_e = 13$, instead of $D/\Delta x = 3$ at $t/T_e = 5$ for $W_e = 110$ and $D/\Delta x = 7$ at $t/T_e = 5$ for $W_e = 19$. For $t/T_e > 13$, PDFs do not evolve anymore. For smaller W_e ($W_e = 2$), the fragmentation process occurs but it does not result in a large distribution of smaller droplets. On the contrary, the main path-connected component is divided in large drops. For this case, coalescence appears later ($t/T_e = 27$) and is less significant. At this time, three main drops are present ($D/\Delta x = 130, 160$ and 180).

As can be seen in these Figs. 9–11, two distinct behaviours are observed with a PDF centered at $D/\Delta x = 10$ for larger W_e, whereas only three main drops are shown for $W_e = 2$. For the larger Weber numbers ($W_e \geqslant 19$) and from $t/T_e \geqslant 13$, we have $D/\Delta x \geqslant 5$ for the wide majority of the droplets, indicating the good spatial resolution of the droplets and the reliability of the DNS simulations.

4.2.2.3. Energy budget.
To understand the role played by surface tension forces in the TKE evolution, an energy budget for TKE (written q in Eq. (9)) is carried out. To do this, a new spatial average conditioned by the level-set function ϕ is introduced. It will be noted $\overline{\cdots}^\phi$ in reference to the conditioning parameter ϕ. Details on the computation of $\overline{\cdots}^\phi$ are given in Fig. 12. Let ϕ_1 be an iso-surface. The points $\mathbf{x}$ of the numerical domain $\mathscr{D}$ such as $\phi(\mathbf{x}) \in [\phi_1; \phi_1 + d\phi]$ ($\phi(\mathbf{x})$ is the level-set function at $\mathbf{x}$) belong to a layer C_1 centered around ϕ_1 whose width is $d\phi$. The average $\overline{\cdots}^\phi(\phi_1)$ is performed among the points which belong to C_1. In our computations, $d\phi$ is of the order of the spatial step.

Thus, using the $\overline{\cdots}^\phi$ average, the equation for the energy budget can be written:

$$\underbrace{\overline{\frac{\partial q}{\partial t}}^\phi}_{\text{I}} + \underbrace{\overline{u_j \frac{\partial q}{\partial x_j}}^\phi}_{\text{III}} = \underbrace{\overline{\frac{\partial}{\partial x_j}(2\mu u_i s_{ij})}^\phi}_{\text{II}} - \underbrace{\overline{\frac{\partial}{\partial x_j}(p u_j)}^\phi}_{\text{IV}} \underbrace{\overline{-2\mu s_{ij} s_{ij}}^\phi}_{\text{V}} + \underbrace{\overline{\rho u_i F_i}^\phi}_{\text{VI}} \qquad (9)$$

where term I is the time rate-of-change, term II is the power of viscous forces, term III is the transport of q, term IV is the power of pressure forces, term V is the dissipation and term VI is the power of interfacial forces $\mathbf{F}$. Here, $\mathbf{F}$ is given by $\mathbf{F} = \sigma \kappa \delta(\phi) \nabla \phi$. In Fig. 13, the different terms of the Eq. (9) are represented vs. time. At each time, the budget is performed on the interface ($\phi = 0$). For example, term I in Fig. 13 is $\overline{\frac{\partial q}{\partial t}}^{\phi=0}(t)$. Every term is normalized with $\epsilon(t)$. A comparison is performed for different W_e numbers. Three kinds of
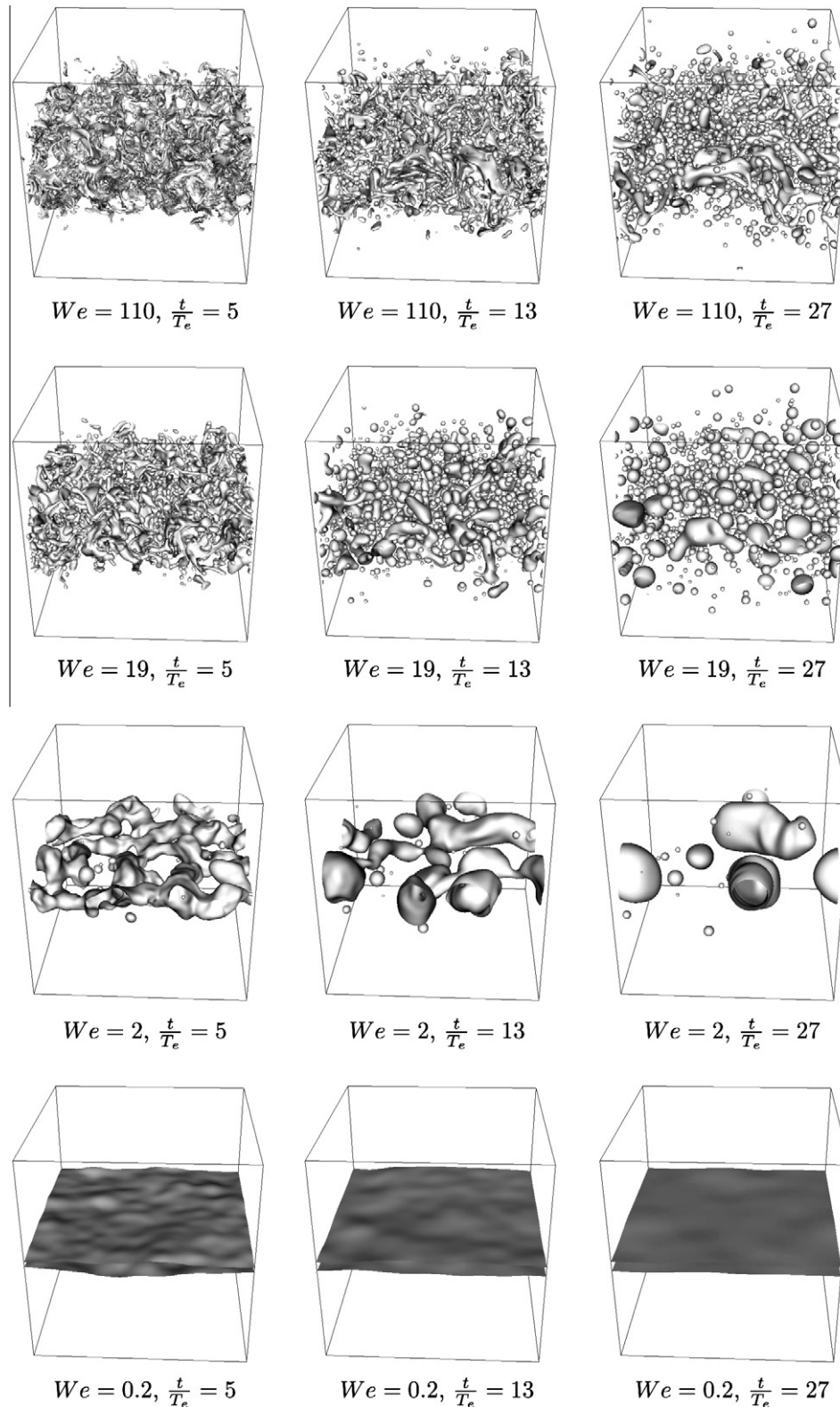
$We = 110, \frac{t}{T_e} = 5$ $We = 110, \frac{t}{T_e} = 13$ $We = 110, \frac{t}{T_e} = 27$

$We = 19, \frac{t}{T_e} = 5$ $We = 19, \frac{t}{T_e} = 13$ $We = 19, \frac{t}{T_e} = 27$

$We = 2, \frac{t}{T_e} = 5$ $We = 2, \frac{t}{T_e} = 13$ $We = 2, \frac{t}{T_e} = 27$

$We = 0.2, \frac{t}{T_e} = 5$ $We = 0.2, \frac{t}{T_e} = 13$ $We = 0.2, \frac{t}{T_e} = 27$

Fig. 8. Liquid sheet represented for four different initial W_e numbers and at three different times.

behaviours can be seen in Fig. 13: the small interfacial scale cases (W_e = 110, 63, 19), the large interfacial scale case (W_e = 0.2) and the transitional one (W_e = 2).

The small interfacial scale cases are related to W_e = 110, 63 and 19 (Fig. 13a–c respectively) where the interfaces present large deformations with small interfacial scales. The predominant scale

is term V (dissipation) but $\frac{\partial q}{\partial t}\big|_{\phi=0} \neq -\epsilon\big|_{\phi=0}$ (or term I ≠ term V), indicating a loss of isotropy at the interface. In Fig. 14, the same budget is carried out for W_e = 110 far from the interface ($\phi/\Delta x$ = 5). Far from the interface, the relation $\frac{\partial q}{\partial t} = -\epsilon$ is verified. This result is the same for every W_e far from the interface. The transport term (III) has a symmetric behaviour compared to the pressure
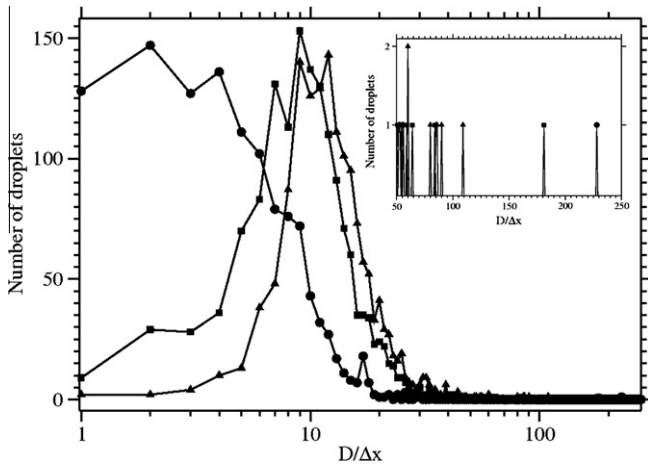
Fig. 9. PDF of the number of droplets vs. the diameter $D/\Delta x$. Δx is the spatial step. W_e = 110. ●: t/T_e = 5; ■: t/T_e = 13 ; ▲: t/T_e = 27. Up-right corner:zoom of the PDF at large $D/\Delta x$ ($\geqslant$50).
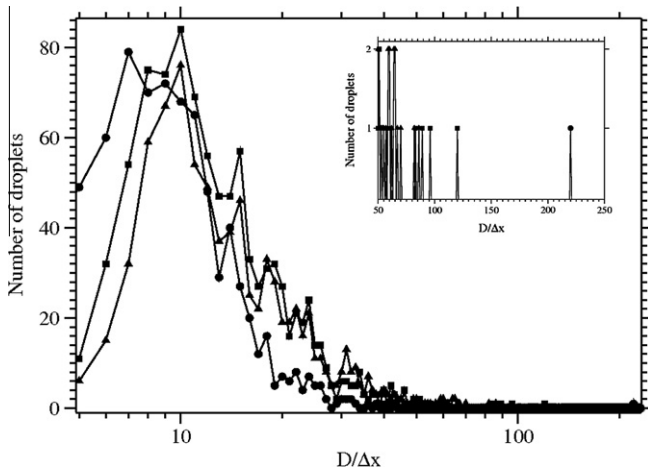
Fig. 10. PDF of the number of droplets vs. the diameter D/Δ_x. Δx is the spatial step. W_e = 19. ●: t/T_e = 5; ■: t/T_e = 13 ; ▲: t/T_e = 27. Up-right corner:zoom of the PDF at large $D/\Delta x$ ($\geqslant$50).
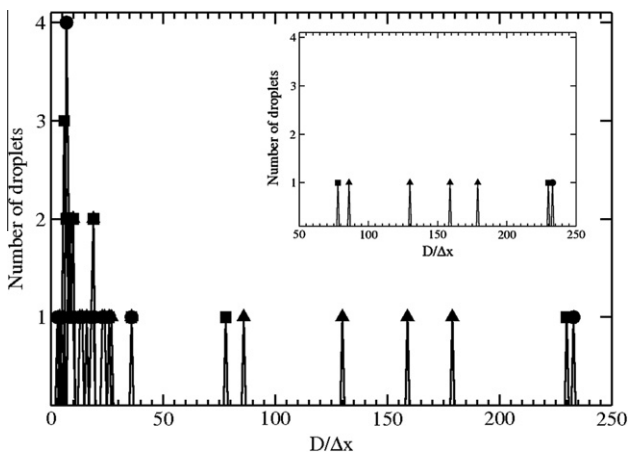

Fig. 11. PDF of the number of droplets vs. the diameter D/Δ_x. Δx is the spatial step. W_e = 2. ●: t/T_e = 5; ■: t/T_e = 13; ▲: t/T_e = 27. Up-right corner:zoom of the PDF at large $D/\Delta x$ ($\geqslant$50).
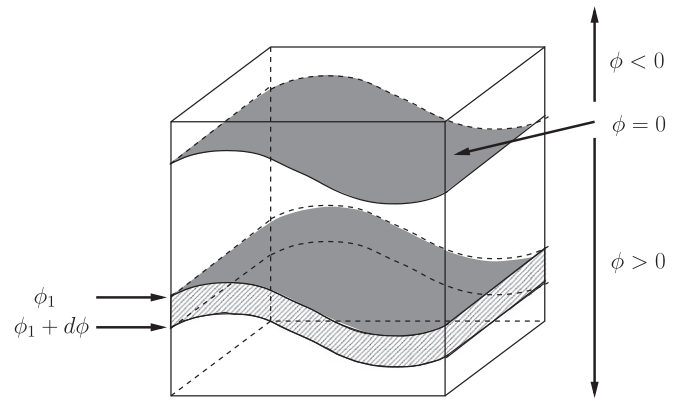

Fig. 12. Geometric layer used for the computation of $\cdot^\phi(\phi_1)$. The interface between the two fluids is represented by the iso-surface ϕ = 0.

term (IV). The two terms are not exactly balanced but have similar behaviours. Back to Fig. 13 for W_e = 110, 63 and 19, term III and term IV have similar behaviours but the magnitude of term IV is stronger than the magnitude of term III resulting in $\frac{\partial q}{\partial t}\big|_{\phi=0} \neq -\epsilon|_{\phi=0}$. The interfacial term (VI) is low. Term VI $\approx u_i\sigma\kappa\|\nabla\phi\|$. As can be seen in Fig. 8, κ can be very large. However, $\sigma_{W_e=110,63,19} \ll 1$ and therefore the product $\sigma\kappa$ is low for W_e = 110,63 and 19, which explains the low magnitude for term (VI). The strength of interfacial forces is driven by the surface tension coefficient σ more than the curvature κ.

The large interfacial scale case is related to W_e = 0.2 (Fig. 13e and f), where the interface remains nearly flat. The previous similitude between the transport term (III) and the pressure term (IV) is not true anymore for W_e = 0.2. For $t/T_e \geqslant 15$, the two predominant terms are the pressure term (IV) and the interfacial term (VI). Their evolutions are comparable and oscillate under a frequency which is consistant with analysis of surface waves given by Lamb (1932):

$$f_{lamb} = \frac{1}{2\pi}\sqrt{\frac{\sigma k^3}{2\rho}} \tag{10}$$

The frequency deduced from Fourier analysis of temporal signal of interfacial energy budget term of Eq. (9), gives a wave length of interfacial instablity of roughly $\pi/2$ which seems to be in good agreement with waves observed in Fig. 8. Therefore, waves observed for W_e = 0.2 in Fig. 8 are surface waves. Pressure and interfacial terms (IV and V) oscillate with the same characteristic frequency given by surface waves on the interface (W_e = 0.2). About the product $\sigma\kappa$, σ is predominant on κ. Indeed, $\kappa \ll 1$ (nearly flat interface) whereas $\sigma \gg 1$ for W_e = 0.2. As can be seen in Fig. 13, the interfacial term VI is high and this is due to high σ.

The transitional case is W_e = 2 (Fig. 13d). For small times, ($t/T_e \leqslant 15$), conclusions are the same as for the small interfacial scale cases (W_e = 110, 63 and 19). For larger times ($t/T_e \geqslant 15$), the interfacial term (VI) increases for $15 \leqslant t/T_e \leqslant 30$. Back to Fig. 8, the curvatures of the large drops do not increase significantly enough from t/T_e = 15 to t/T_e = 30 to raise the term VI. The large drops oscillate from t/T_e = 15 to t/T_e = 30 under the competition of two contributions: turbulence which imposes deformations to the interface and surface tension forces which play the role of a restoring force. These oscillations cause increases of local velocities near the interface inducing the increase of the term VI on the interface. Viscosity damps oscillations: as turbulence intensity decays in time, the drops keep their spherical shapes and local velocities in the neighbourhood of the interface decrease, which explains the decrease of the term VI from t/T_e = 30. Note that dissipation (term V) is larger than for other W_e.
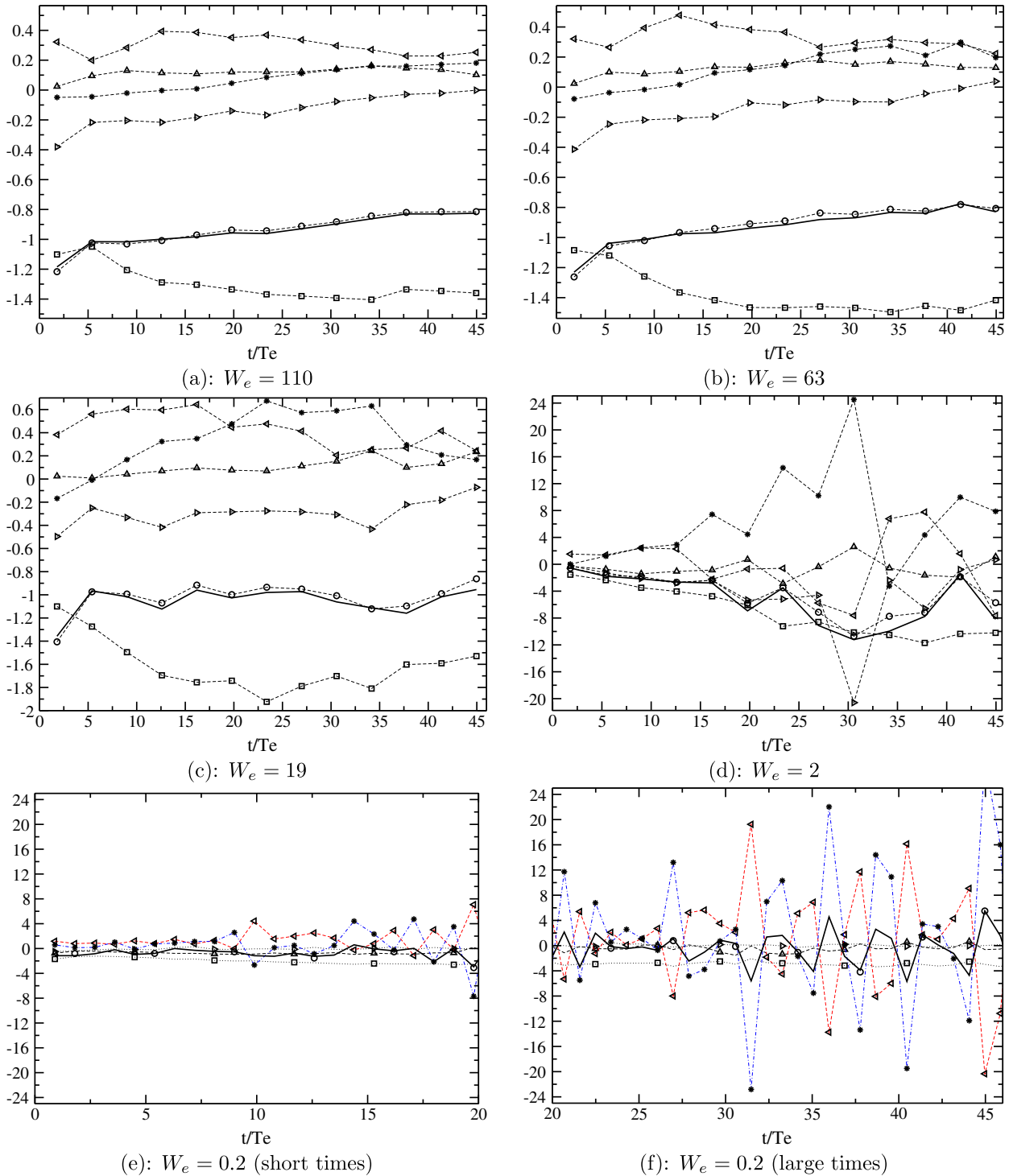
Fig. 13. Energy budget. ○, time rate-of-change (term I); △, viscous terms (term II); ▷, transport (term III); ◁, pressure terms (term IV); □, dissipation (term V); ∗, interfacial term (term VI); solid line, sum of terms II–VI. See Eq. (9) for the different terms. Every term is normalized by $\epsilon(t)$.

4.2.2.4. Temporal evolution of TKE: W_e influence. In Fig. 15, the time evolution of normalized TKE $(q - q_\infty)/q_\infty$ is represented for different W_e numbers. q_∞ is the TKE of the reference case ($\sigma = 0$).

At early stages of the simulations ($t/T_e < 6$), $(q - q_\infty)/q_\infty < 0$ for all Weber numbers showing that TKE decreases faster when $W_e < \infty$. This decrease is greater as the surface tension coefficient increases. TKE is transfered from the fluid flow to the interface. Energy is used to break the interface into smaller pieces. For $W_e = 0.2$ where σ is high enough to prevent the interface from breaking, energy is used from TKE to cause deformations of the interface with surface waves.

For later times, $(q - q_\infty)/q_\infty$ increases for all W_e numbers. Three different behaviours can be observed: small scale cases ($W_e = 110$, 63, 19), large scale scales ($W_e = 0.2$) and the transitional case ($W_e = 2$).

- For small scale cases ($W_e = 110$, 63, 19) $(q - q_\infty)/q_\infty$ increases but remains negative. The interface is finely grained, consisting of small filaments and droplets (Fig. 8), where the interfacial energy is used for coalescence and creation of larger interfacial structures. Even for later times, $(q - q_\infty)/q_\infty$ remains negative
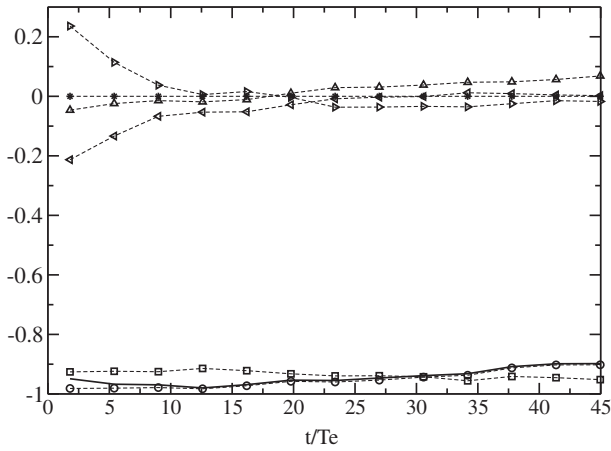
Fig. 14. Energy budget far from the interface. $W_e = 110$. $\circ$, time rate-of-change (term I); $\triangle$, viscous terms (term II); $\triangleright$, transport (term III); $\triangleleft$, pressure terms (term IV); $\square$, dissipation (term V); $\ast$, interfacial term (term VI); solid line, sum of terms II-VI. See Eq. (9) for the different terms. Every term is normalized by $\epsilon(t)$.
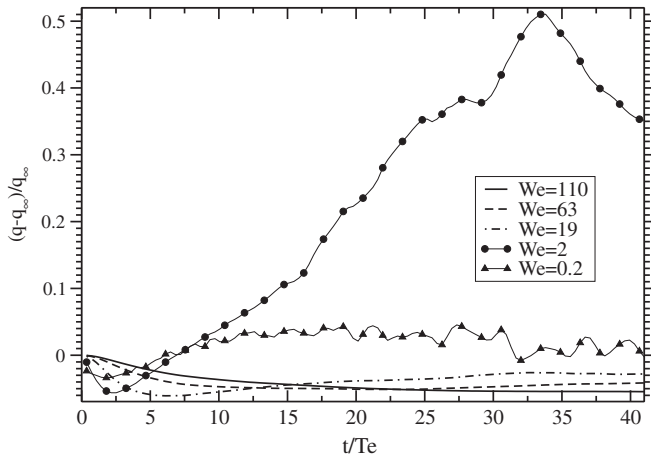

Fig. 15. Time evolution of turbulent kinetic energy (TKE) for different W_e. q_∞ is TKE for $W_e = \infty$.

showing a loss for TKE compared to single-phase case ($W_e = \infty$). In that cases, at large times, coalescence and break-up are important (see Fig. 8), which explains TKE loss for two-phase interactions.

- For the transitional case ($W_e = 2$), $q - q_\infty$ becomes positive $\left(\frac{t}{T_e} \geqslant 7\right)$. Unlike previous cases, large non spherical blobs are observed. Under surface tension forces these blobs keep oscillating without merging throughout the simulation. In this case the distance in between is significantly larger than for $W_e \geqslant 19$. These oscillations explain the increase of $(q - q_\infty)/q_\infty$ as q_∞ vanishes up to $t/T_e = 30$. For $t/T_e \geqslant 30$, $(q - q_\infty)/q_\infty$ decreases. It can be explained back to Fig. 13 where it was shown that large drops stop oscillating from $t/T_e = 30$.

- For the large scale case ($W_e = 0.2$), $q - q_\infty$ become positive $\left(\frac{t}{T_e} \geqslant 6\right)$. Due to high surface tension coefficient, the sheet remains unbroken and is only disturbed by surface waves. These surface waves are a gain for TKE but are damped by viscosity. Therefore, for large times, $q - q_\infty$ decreases. As q_∞ decreases too, the ratio $(q - q_\infty)/q_\infty$ shows a stage for $W_e = 0.2$ at large times.

4.2.2.5. Turbulent statistics.

In Fig. 16 and 17, normal and tangential Reynolds stress profiles are represented vs. $\frac{\phi}{\delta}$ where ϕ is the level-set function (signed distance function to the interface) and δ is the initial thickness of the sheet. More precisely, if $\mathbf{n}$ and $\boldsymbol{\tau}$ are respectively the local unit normal and tangential vectors, and if u'_n and u'_τ are given by

$$\begin{aligned} u'_n &= \mathbf{u}' \cdot \mathbf{n} \\ u'_\tau &= \mathbf{u}' \cdot \boldsymbol{\tau} \end{aligned} \tag{11}$$

then Figs. 16 and 17 represent respectively $\overline{u_n'^2}^\phi\left(\frac{\phi}{\delta}\right)$ and $\overline{u_\tau'^2}^\phi\left(\frac{\phi}{\delta}\right)$. Using ϕ enables representing Reynolds stress profiles in function of the signed distance to the interface. $\overline{u_n'^2}^\phi\left(\frac{\phi}{\delta}\right)$ and $\overline{u_\tau'^2}^\phi\left(\frac{\phi}{\delta}\right)$ are normalized by their respective averaged values far from the interface $\frac{\phi}{\delta} \gg 1$. In Figs. 16 and 17 oscillations appear far from the interface. A way to improve the resolution is the use of ensemble averaging in addition to the spatial averaging. To do this, each realization has to be produced by running the simulation under the same flow parameters but with different initial conditions. Because of prohibitive CPU times with 512^3 grids, such ensemble averagings have not been performed.

Figs. 16 and 17 show two main trends. At short times $\left(\frac{t}{T_e} \leqslant 2\right)$ for $0 \leqslant \frac{\phi}{\delta} \leqslant 1$ a loss for $\overline{u_n'^2}^\phi$ can be seen near the interface whereas a gain for $\overline{u_\tau'^2}^\phi$ occurs. Every W_e number is concerned by this phenomenon. Near the interface a transfer of energy happens from $\overline{u_n'^2}^\phi$ to $\overline{u_\tau'^2}^\phi$. Perot and Moin (1995) study turbulence in the presence of different boundary conditions (idealized permeable wall, idealized free surface, solid wall) to highlight the effects of wall blocking and the role of *splat* events. According to Perot and Moin (1995), intercomponent energy transfers are due to an imbalance between *splat* and *antisplat* events. For Perot and Moin (1995), this imbalance is controlled by viscosity. According to Walker et al. (1996), this imbalance is the consequence of both the blocking effect of the interface and a return-to-isotropy phenomenon to reduce anisotropy due to the interface. In the case of an ideal free surface, Perot and Moin (1995) show a local increase for $\overline{u_\tau'^2}^\phi$ and a decrease for $\overline{u_n'^2}^\phi$ near the free surface. In Figs. 16 and 17 the same mechanism is observed for $\frac{t}{T_e} \leqslant 2$. Therefore for early times, anisotropy spreads around the interface on a thickness of δ and the energy transfer from turbulence to the interface induces anisotropy in the vicinity of the interface.

At larger times $\left(\frac{t}{T_e} \geqslant 5\right)$, except for $W_e = 2$ and $W_e = 0.2$, both $\overline{u_n'^2}^\phi$ and $\overline{u_\tau'^2}^\phi$ decrease near the interface. The previous intercomponent energy transfer from $\overline{u_n'^2}^\phi$ to $\overline{u_\tau'^2}^\phi$ due to the presence of the interface is not observed any more. $W_e = 2$ appears to be a transitional case from the previous conclusions. Large spherical blobs keep oscillating under surface tension forces without merging. In this case, for larger times $\left(\frac{t}{T_e} \geqslant 5\right)$, the interface behaves like a generator for turbulence imposing local increase for both $\overline{u_n'^2}^\phi$ and $\overline{u_\tau'^2}^\phi$ near the interface (Figs. 16 and 17). For $W_e = 0.2$, at larger times $\left(\frac{t}{T_e} \geqslant 5\right)$, a decrease of $\overline{u_n'^2}^\phi$ is observed near the interface $\left(\frac{\phi}{\delta} \leqslant 2\right)$ whereas the tangential Reynolds stresses $\overline{u_\tau'^2}^\phi$ increase. Looking back at Fig. 8 the sheet remains unbroken and is only disturbed by surface waves for $W_e = 0.2$. The topological configuration of the sheet is similar to a free plane surface. In Perot and Moin (1995) the study of turbulence interacting with an ideal free plane surface concludes with the local increase of $\overline{u_\tau'^2}^\phi$ and decrease of $\overline{u_n'^2}^\phi$ near the free surface. Therefore an analogy between the sheet and an ideal free plane surface can be done in the case of small W_e numbers at large times.

In Fig. 18, vorticity intensity Ω_ϕ is represented as a function of ϕ, the signed distance function. $\Omega_\phi(\phi)$ have to be understood as follows:

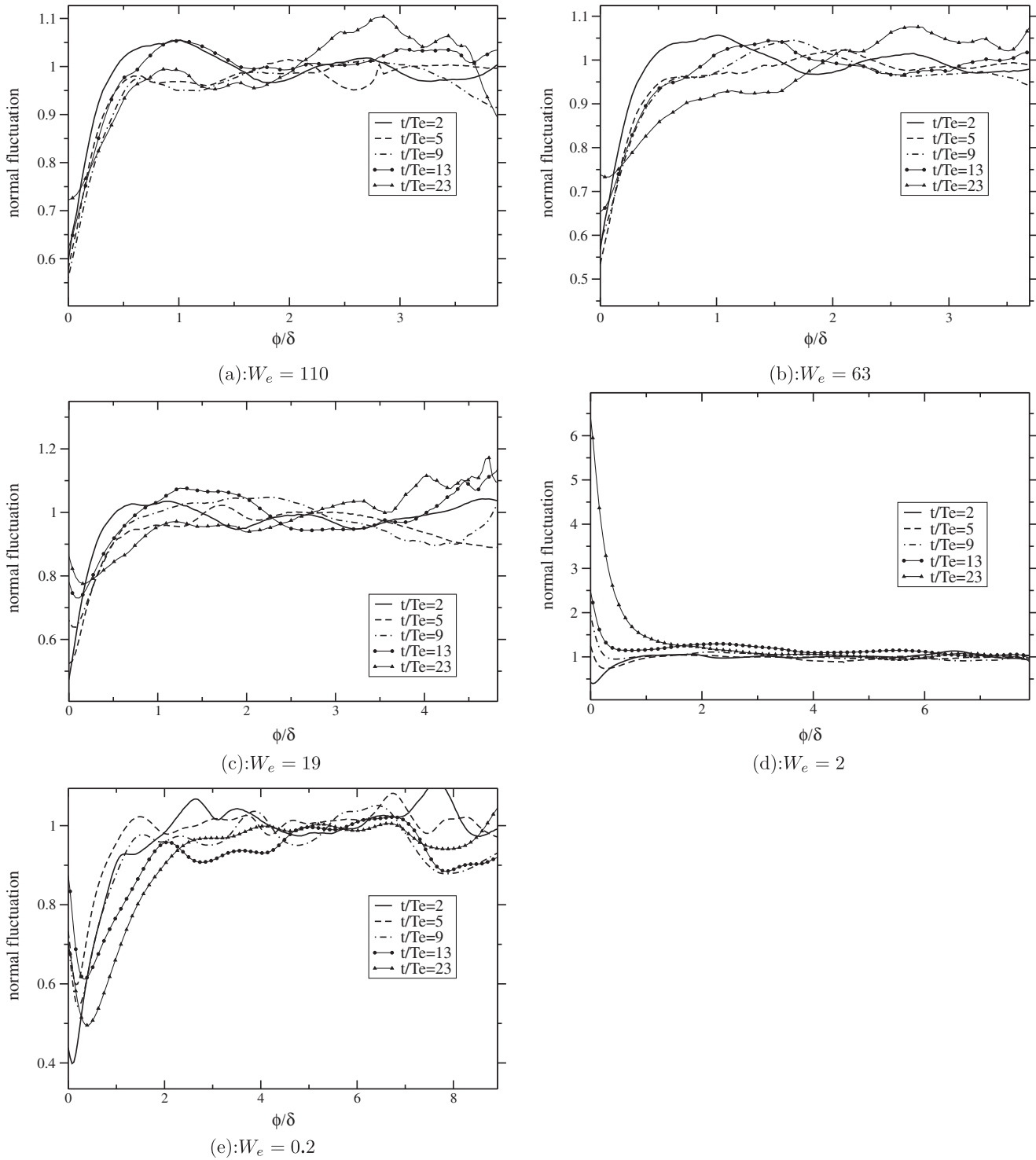$$\Omega_\phi(\phi) = \sqrt{\overline{\|\mathbf{\Omega}\|^2}^\phi} \tag{12}$$

(a):$W_e = 110$

(b):$W_e = 63$

(c):$W_e = 19$

(d):$W_e = 2$

(e):$W_e = 0.2$

Fig. 16. Normal Reynolds stresses vs. ϕ for different W_e at different $\frac{t}{T_e}$.

where $\boldsymbol{\Omega} = \nabla \wedge \mathbf{u}$. Ω_ϕ is normalized by its value far from the interface. In all cases vorticity is generated near the interface ($\frac{\phi}{\delta} \leqslant 1$). Vorticity is generated quickly and its spreading remains close to the interface (in a zone from 0 to δ around the interface) even for large times. The magnitude of the vorticity peak increases in time and is maximum for $W_e = 2$ which corresponds to the transitional case (see Fig. 8). This vorticity peak is the result of the interface/turbulence interaction.

In this study, it was shown that the interface/turbulence interaction causes anisotropy in the vicinity of the interface. This anisotropy has a universal behaviour for every W_e number at early stages when an energy transfer from turbulence to the interface occurs. Normal Reynolds stresses decrease whereas tangential ones increase. At larger times, less obvious conclusions about the behaviour of both normal and tangential Reynolds stresses can be drawn. This local anisotropy will have to be taken into consideration when developing LES models for subgrid scale terms deriving from the interface/turbulence interaction. For such models, the isotropy hypothesis cannot be assumed anymore.
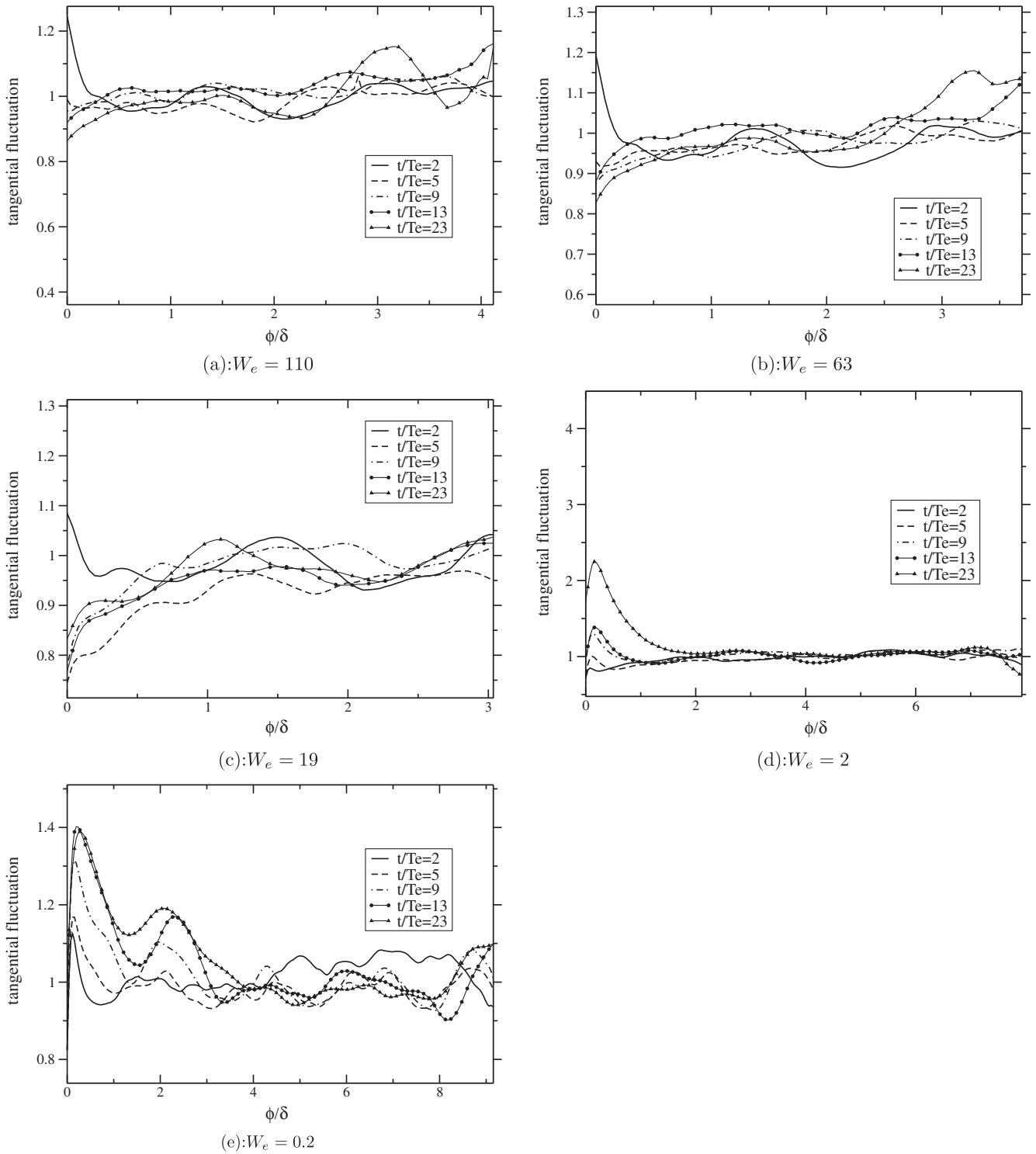
Fig. 17. Tangential Reynolds stresses vs. ϕ for different W_e at different $\frac{t}{T_e}$.

4.2.3. 3D energy spectra

In this section, a spectral analysis is carried out to identify the scales where the interface/turbulence coupling appears. 3D energy spectra are plotted and results are summarized in Fig. 19. For five W_e numbers, energy spectra are compared with the reference case $W_e = \infty$. Comparisons are performed for different $\frac{t}{T_e}$ (from 3 to 30). In the dimensionless wavenumber $k\eta$, the Kolmogorov length scale η is the one of the single-phase configuration chosen at $t/T_e = 3$ for every time. At early stages, when $\frac{t}{T_e} < 3$, spectral behaviours for

single- and two-phase cases are nearly the same. However, for later times, clear differences can be observed. Energy contained at small turbulent scales (high wave numbers $k\eta > 0.2$) is higher than for $W_e = \infty$ (single-phase case). Therefore the interface appears to be an energy generator for the small scales of turbulence. This energy gain which is spectrally limited to the highest wavenumbers is the result of an energy transfer. To quantify this energy redistribution, a kinetic energy budget is carried out. To set notations, a diagram is drawn in Fig. 20 to summarize configurations shown
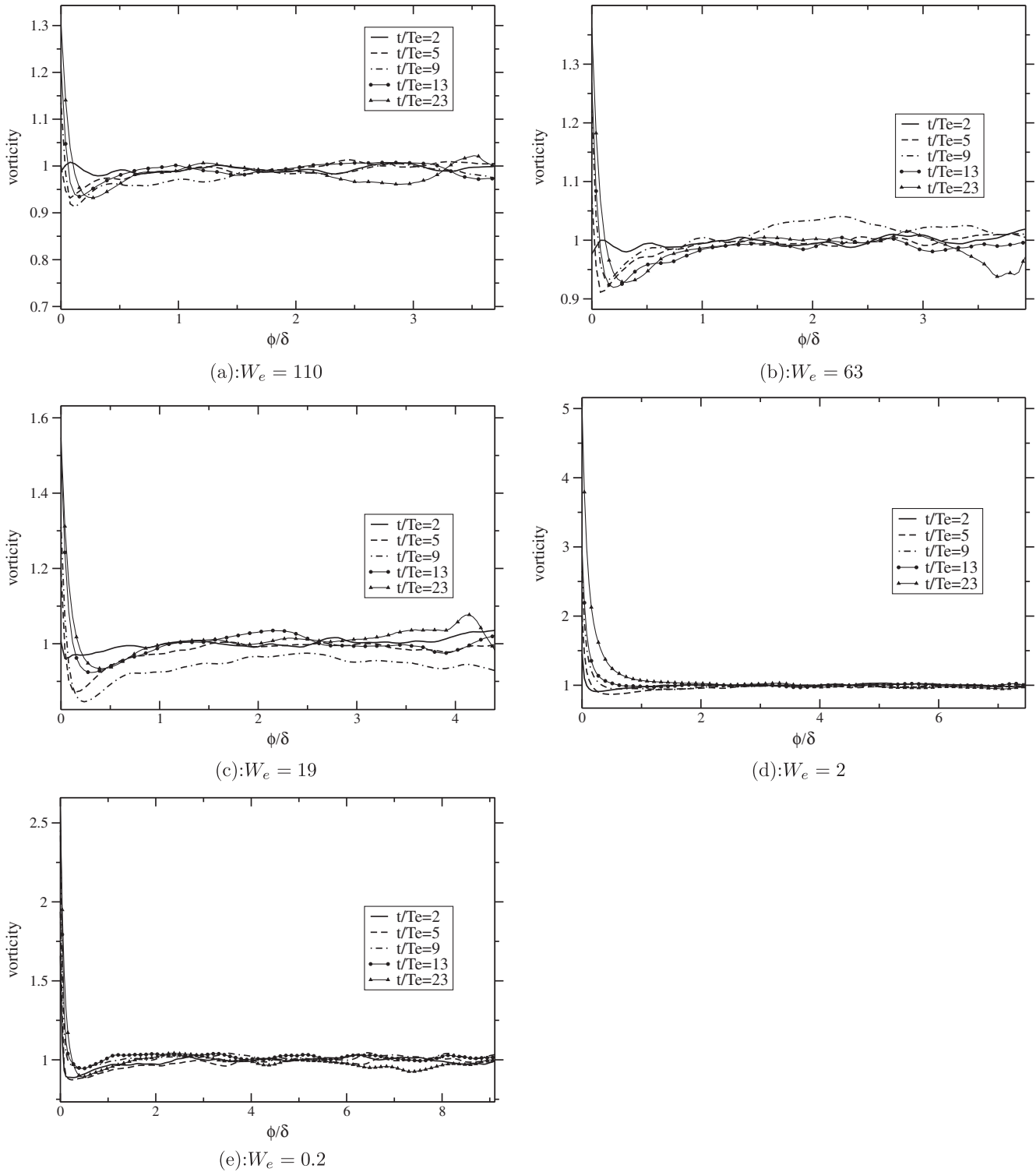
Fig. 18. Vorticity vs. ϕ for different W_e at different $\frac{t}{T_e}$.

in Fig. 19. In Fig. 20 two 3D energy spectra are plotted. The first one corresponds to the reference case ($W_e = \infty$) whereas the other one is drawn for ($W_e < \infty$). k_{max} is the maximum wave number simulated, while $k_c(W_e)$ is the wave number at which the intersection between the two spectra occurs. Wave number k_c depends on W_e. The energy contained in the large scales of turbulence is given by calculating $I_1 = \int_0^{k_c} E(k)\,dk$. The energy contained in the small ones is given by $I_2 = \int_{k_c}^{k_{max}} E(k)\,dk$. The total TKE is given by

$I_3 = \int_0^{k_{max}} E(k)\,dk$. Results are given in Table 2. In this table ϵ means that the magnitude was too low to be considered as significant. Symbol $\emptyset$ means it was not possible to determine a single value for k_c and then to perform an accurate budget between small and large scales. For every time and for every $W_e < \infty$, energy I_1 is lower than for $W_e = \infty$ (single-phase). Therefore the interface damps TKE deriving from the larger scales (low wavenumbers). The damping is stronger as the surface tension coefficient is higher (low W_e
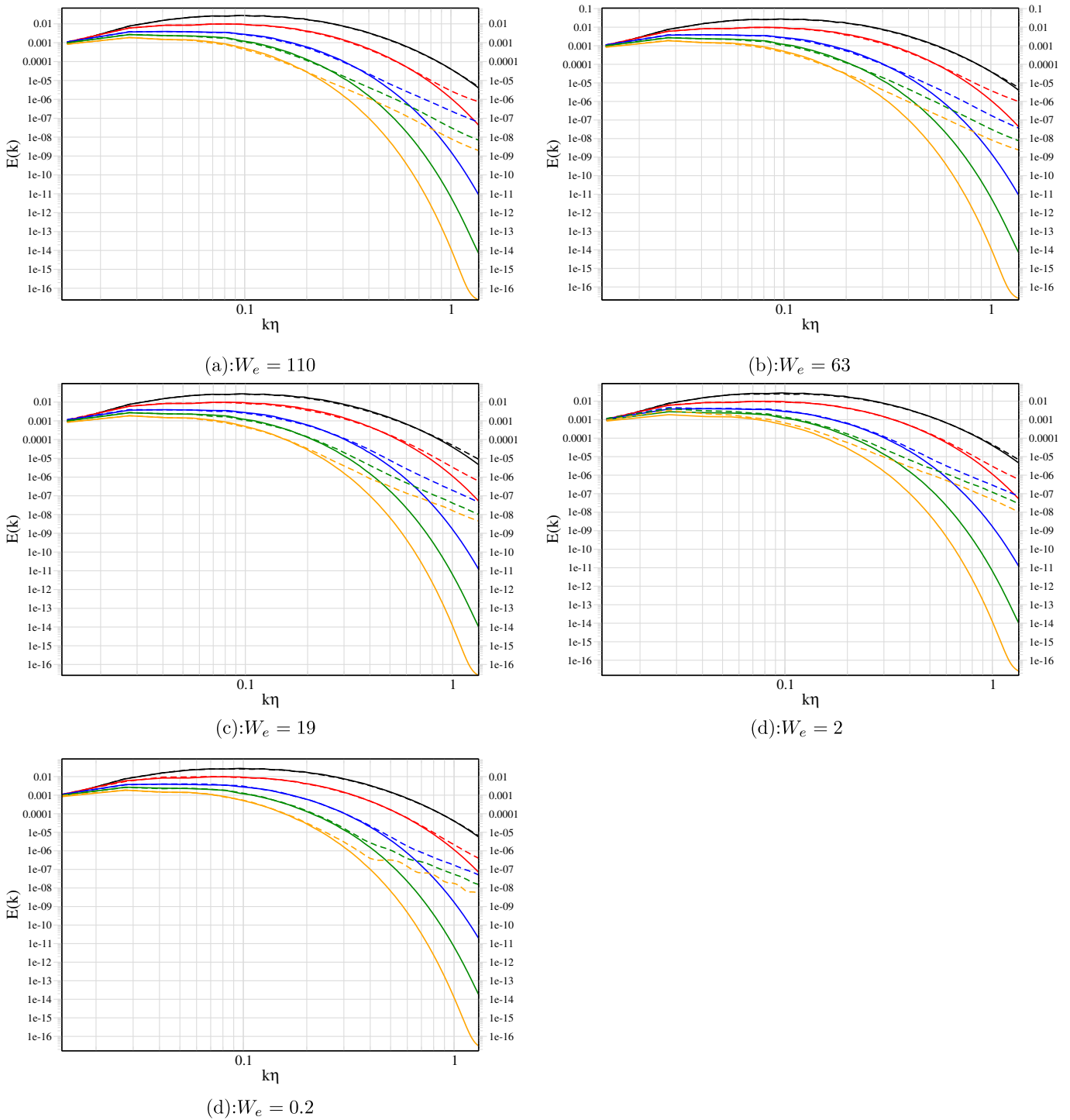
(a): $W_e = 110$

(b): $W_e = 63$

(c): $W_e = 19$

(d): $W_e = 2$

(d): $W_e = 0.2$

Fig. 19. 3D energy spectra. Solid line: $W_e = \infty$. Dashed line: $W_e < \infty$. Black: $\frac{t}{T_e} = 3$. Red: $\frac{t}{T_e} = 6$. Blue: $\frac{t}{T_e} = 13$. Green: $\frac{t}{T_e} = 20$. Orange: $\frac{t}{T_e} = 30$. 512^3 grid. η is the Kolmogorov length scale at $t/T_e = 3$. (For interpretation of the references to colour in this figure legend, the reader is referred to the web version of this article.)

number). Concerning small turbulent scales, energy I_2 is higher for every $W_e < \infty$ than for $W_e = \infty$, indicating the interface plays a generator role for the smallest turbulent scales. Therefore there is an energy transfer from the turbulent largest scales to the smallest ones for $W_e < \infty$. Except for $W_e = 2$ at large times, I_3 is lower for $W_e < \infty$ than for $W_e = \infty$. So the damping of the largest scales is more important than the increase of the smallest ones resulting in a global decrease of the TKE due to surface tension forces. For $W_e = 2$ at large times, the global increase of the TKE has been previously explained. Referring back to Fig. 19 the energy transfer

from the largest to the smallest turbulent scales is all the more significant as $\frac{t}{T_e}$ is high. The transfer is effective from $\frac{t}{T_e} > 3$ at a time when the interface/turbulence interaction is significant. For $\frac{t}{T_e} \in [0;3]$ the interface has no impact on the spectral distribution of the turbulent energy.

In the case of large W_e where the interface is finely grained at large times ($t/T_e \geqslant 13$), the droplet size distribution is correlated with the local TKE increase for the small scales. Back to Fig. 9 and 10 for $W_e = 110$ and $W_e = 19$, the wide majority of droplets have their diameters D such as $D/\Delta x \leqslant 30$, which corresponds to
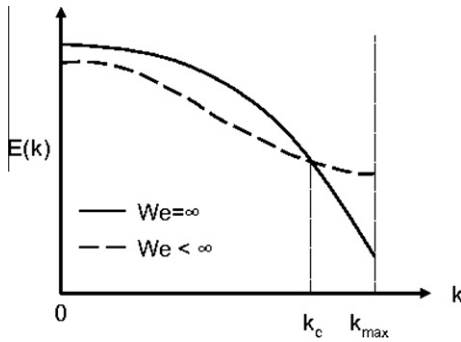
Fig. 20. Synthesis scheme of the configurations in Fig. 19.

Fig. 21. $\alpha(z)$ vs. z/L_b. L_b is the box size. $\frac{t}{T_e} = 13$.

$0.23 \leqslant k\eta_{|t/T_e=3}$. In Fig. 19, it can be seen that scales for which TKE increases are such as $k\eta_{|t/T_e=3} \geqslant 0.2$. Therefore, for the cases where the interface is finely grained (W_e = 110, 63 and 19), the energy transfer occurs at the typical scales given by the droplets where the interface/turbulence energy transfers are predominant.

The energy transfer has to be taken into consideration in the development of future LES models. The subgrid contribution of the interface/turbulence coupling is an increase of the TKE budget deriving from the smallest scales. A first step is the validation of existing LES models concerning the treatment of the subgrid contribution of interface/turbulence coupling.

4.2.4. Distance to the interface and 2D energy spectra

The energy transfer from the large turbulent scales to the small ones has been previously established for the whole computational domain. Now the distance to the interface is taken into account. To do that, the computational box is divided into 10 planes which are parallel to the initial sheet. $\mathbf{e_z}$ is the normal unit vector to the 10 planes. Let $\alpha(\tilde{z})$ be the density function of the phase $\phi < 0$ at $z = \tilde{z}$. If $\alpha(\tilde{z}) = 0$ then the plane $z = \tilde{z}$ is totally outside the sheet. If $\alpha(\tilde{z}) = 1$ then the plane $z = \tilde{z}$ is totally inside the sheet. And if $0 < \alpha(\tilde{z}) < 1$ then the plane $z = \tilde{z}$ crosses the interface. In Fig. 21, $\alpha(z)$ is represented vs. z/L_b for different W_e numbers and at $\frac{t}{T_e} = 13$. The initial sheet (at $t = 0$) spreads from $z = -0.025L_b$ to $z = +0.025L_b$. In Fig. 21, the positions of the 10 planes are represented too. Because of obvious symmetries only the planes 1–5 will be studied. Conclusions are similar for planes from 6 to 10. The
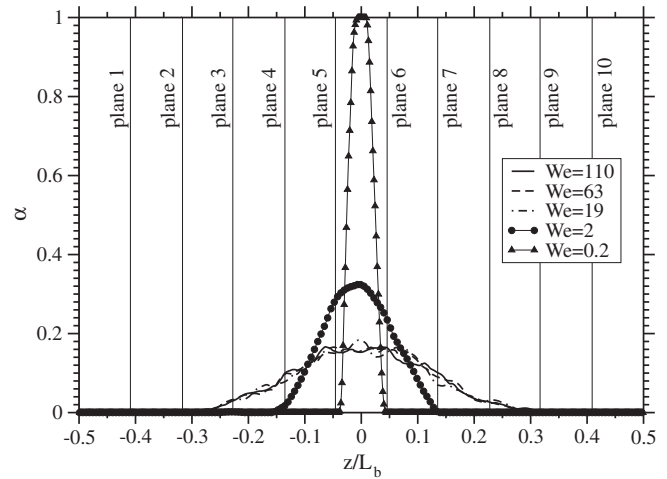
plane 1 is the farthest plane from the interface. The plane 5 is the nearest one. As can be seen in Fig. 21, whatever the Weber number is, the two first planes (planes 1 and 2) never cross the interface. The planes 3 and 4 cross the interface for W_e = 110, 63 and 19. For W_e = 2, the only plane which crosses the interface is the plane 5 and the other planes are all out of the sheet. For W = 0.2 none of the planes crosses the interface. Because of a strong surface tension coefficient, the sheet has little deformations and the interface is parallel to every planes.

In Fig. 22, 2D energy spectra are plotted for different W_e at $\frac{t}{T_e} = 13$. Two dimensional spectra are performed in planes 1–5. The closer to the interface spectra are performed, the higher the energy of small scales is. The energy transfer from the larger turbulent scales to the smaller ones is stronger as one moves towards the interface. For W_e = 110, 63 and 19, planes 4 and 5 are the planes where the energy transfer is the strongest. For these W_e numbers, α = 0.1 for plane 4 and α = 0.16 for plane 5 (Fig. 21). Therefore, in these two planes, both phases $\phi < 0$ and $\phi > 0$ are found and interactions are strong via the interface. In Fig. 22, for W_e = 2, the energy transfer between large and small scales is significant only in the plane 5. Once again, this is consistent with Fig. 21 where the plane

Table 2
Energy repartition between small and large scales of turbulence for different W_e numbers at different times.

$\frac{t}{T_e}$	W_e	$I_1 = \int_0^{k_c} E(k)\,dk$	$I_2 = \int_{k_c}^{k_{max}} E(k)\,dk$	$I_3 = \int_0^{k_{max}} E(k)\,dk$	$\frac{I_1}{I_3}$	$\frac{I_2}{I_3}$
3	∞	6.03×10^{-3}	1.00×10^{-5}	6.04×10^{-3}	0.998	0.002
	110	5.96×10^{-3}	1.00×10^{-5}	5.97×10^{-3}	0.998	0.002
	63	5.91×10^{-3}	1.00×10^{-5}	5.92×10^{-3}	0.998	0.002
	19	5.72×10^{-3}	6.00×10^{-5}	5.78×10^{-3}	0.990	0.01
	2	5.66×10^{-3}	6.00×10^{-5}	5.72×10^{-3}	0.990	0.01
6	∞	1.75×10^{-3}	ϵ	1.75×10^{-3}	$1 - \epsilon$	ϵ
	110	1.70×10^{-3}	1.00×10^{-5}	1.71×10^{-3}	0.994	0.006
	63	1.67×10^{-3}	1.00×10^{-5}	1.68×10^{-3}	0.994	0.006
	19	1.61×10^{-3}	4.00×10^{-5}	1.65×10^{-3}	0.976	0.024
	2	1.65×10^{-3}	8.00×10^{-5}	1.73×10^{-3}	0.954	0.046
13	∞	4.75×10^{-4}	3.00×10^{-6}	4.78×10^{-4}	0.994	0.006
	110	4.54×10^{-4}	4.00×10^{-6}	4.58×10^{-4}	0.991	0.009
	63	4.48×10^{-4}	6.00×10^{-6}	4.54×10^{-4}	0.987	0.013
	19	4.36×10^{-4}	1.8×10^{-5}	4.54×10^{-4}	0.960	0.04
	2	$\emptyset$	$\emptyset$	5.13×10^{-4}	$\emptyset$	$\emptyset$
20	∞	2.29×10^{-4}	2.00×10^{-6}	2.31×10^{-4}	0.991	0.009
	110	2.17×10^{-4}	3.00×10^{-6}	2.20×10^{-4}	0.986	0.014
	63	2.14×10^{-4}	5.00×10^{-6}	2.19×10^{-4}	0.977	0.023
	19	2.11×10^{-4}	1.10×10^{-5}	2.22×10^{-4}	0.95	0.05
	2	$\emptyset$	$\emptyset$	2.85×10^{-4}	$\emptyset$	$\emptyset$

5 is the only plane which crosses the interface. In Fig. 22, the same conclusions can be drawn for $W_e = 0.2$: none of the planes crosses the interface and therefore the energy transfer between large and small scales is not observed. For $W_e = 0.2$, even plane 5 is too far from the interface, and the interface/turbulence interaction is really restricted to a thin area around $\phi = 0$. Fig. 22 shows that the energy transfer from the large to the small scales is spatially limited to the vicinity of the interface.

The spectral spreading of the energy transfer is now investigated. To do so, the ratio $\frac{E(k,W_e=19,t)}{E(k,W_e=\infty,t)}$ is performed for several wave numbers k and different times. $W_e = 19$ is chosen to carry out the study and similar conclusions could be drawn for the other W_e numbers. In Fig. 23, for $\frac{t}{T_e} = 5$, $\frac{E(k)_{W_e=19}}{E(k)_{W_e=\infty}} \gg 1$ for high wave numbers (for $k\eta_k > 1.5$) and only the smallest scales of turbulence get energy from the energy transfer previously explained. For later times
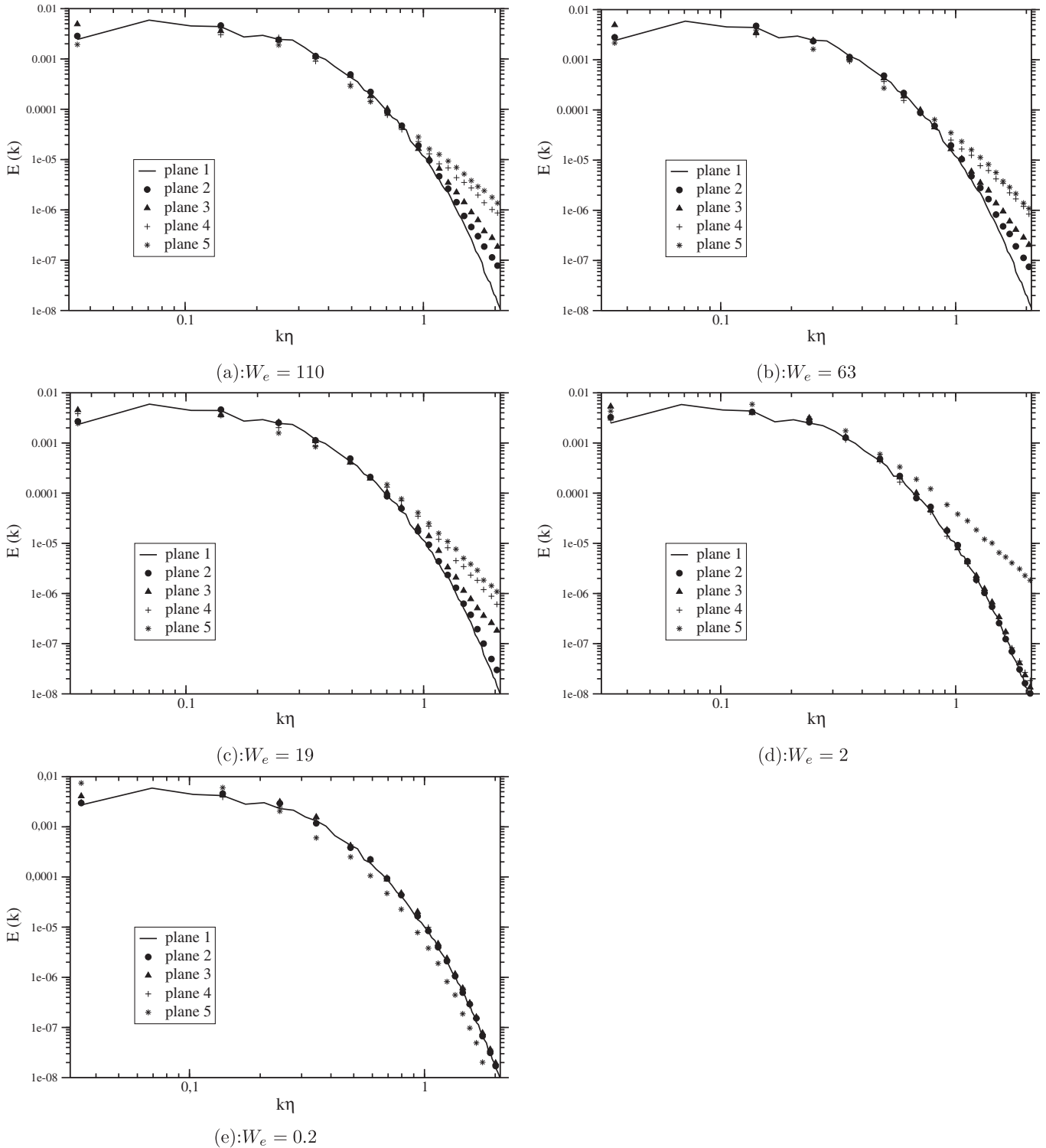

(a):$W_e = 110$

(b):$W_e = 63$

(c):$W_e = 19$

(d):$W_e = 2$

(e):$W_e = 0.2$

Fig. 22. 2D energy spectra. Planar splitting. $\frac{t}{T_e} = 13$.
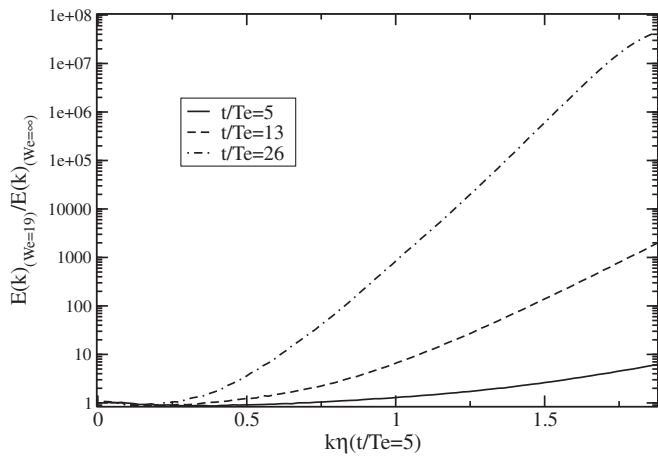
Fig. 23. $\frac{E(k)_{W_e=19}}{E(k)_{W_e=\infty}}$ at different $\frac{t}{T_e}$.

$\left(\frac{t}{T_e} = 13 \text{ and } 26\right)$, $\frac{E(k)_{W_e=19}}{E(k)_{W_e=\infty}} \gg 1$ for $k\eta_k > 1$. Therefore larger and larger scales get energy in the transfer from large to small turbulent scales indicating a spectral spreading of the energy transfer.

5. Conclusion

This work aimed at providing a first contribution to the understanding of the coupling between turbulence and capillary effects. A decaying HIT flow was chosen to carry out this study. A first step was to calibrate the HIT flow to get relevant statistics about isotropy, length scales and turbulent parameters. Then, an initially plane sheet was added in the computational domain and a parametric study on the surface tension coefficient (Weber number) was carried out. For the first time, DNS results have been obtained to point out anisotropic interaction between turbulence and an interface with wide deformations. From a qualitative point of view, two types of turbulence/interface interactions have been observed with a transitional case. For large W_e numbers, the interface is torn off under inertial forces. The interface is finely grained and in this case, the energy transfer from turbulence to the interface is used for the coalescence of small droplets into larger drops under surface tension forces. For large W_e at early times, an increase of the tangential Reynolds stresses is observed near the interface whereas the normal ones decrease. For later times, both normal and tangential Reynolds stresses decrease. An energy transfer from the large scales to the small ones is noticed. This transfer is predominant in the vicinity of the interface and driven by the scales of the small droplets. As W_e decreases, a transitional case has been observed which is still grained. Drops are large enough to be independant from the other neighbouring droplets. In this case, the interfacial energy initially involved by the turbulent flow is given back to the fluid surrounding the interface and amplified by the surface tension forces. For lower W_e numbers, the interface remains flat and oscillates under surface waves. The characteristic frequency of surface waves is observed in the TKE budget. For every W_e number, anisotropy and vorticity appear in the vicinity of the interface resulting from the turbulence/interface interaction. For the development of LES two-phase flow models, this work will continue recent works of Labourasse et al. (2007), Liovic and Lakehal (2007b), Vincent et al. (2008) and will allow the development of sub-grid scale models which will take into account the coupling between surface tension forces and turbulence.

Acknowledgements

References

De Angelis, V., 1998. Numerical Investigation and Modelling of Mass Transfer Processes at Sheared Gas–liquid Interface. PhD Thesis, UCSB.

Banerjee, S., Lakehal, D., Fulgosi, M., 2004. Surface divergence models for scalar exchange between turbulent streams. Int. J. Multiface Flow 30, 963–977.

Borue, V., Orszag, S.A., Staroselsky, I., 1995. Interaction of surface waves with turbulence: direct numerical simulations of turbulent open-channel flow. J. Fluid Mech. 286, 1–23.

Boughanem, H., Trouvé, A., 1996. Validation du code de simulation directe 'NTMIX3D' pour le calcul des écoulements turbulents réactifs. Technical Report 42907, Institut Français du Pétrole.

Bunner, B., Tryggvason, G., 2003. Effect of bubble deformation on the properties of bubbly flows. J. Fluid Mech. 495, 77–118.

Chorin, A.J., 1968. Numerical solution of the Navier–Stokes equations. Math. Comput. 22, 745–762.

Couderc, F., 2007. Développement d'un code de calcul pour la simulation d'écoulements de fluides nonmiscibles. Application à la désintégration assistée d'un jet liquide par un courant gazeux. PhD thesis, Ecole nationale supérieure de l'aéronautique et de l'espace.

Delhaye, J., 1974. Jump conditions and entropy sources in two-phase systems. Local instant formulation. Int. J. Multiface Flow 1, 395–409.

Fedkiw, R., Liu, X., Kang, M., 2000. A boundary condition capturing method for Poisson's equation on irregular domains. J. Comput. Phys. 160, 151–178.

Fulgosi, M., Lakehal, D., Banerjee, S., DeAngelis, V., 2003. Direct numerical simulation of turbulence in a sheared air–water flow with deformable interface. J. Fluid. Mech. 482, 319–345.

Handler, R.A., Swean, T.F., Leighton, R.I., Swearingen, J.D., 1993. Length scales and the energy balance for turbulence near a free surface. AIAA J. 31 (11), 1998–2007.

Harlow, F.H., Welsh, J.E., 1995. Numerical calculation of time dependent viscous incompressible flow with free surface. Phys. Fluids 8, 21–82.

Howarth, L., Karman, T., 1938. On the statistical theory of isotropic turbulence. Proc. Roy. Soc. Gottingen Nachrichte A164 (917), 192–215.

Jiang, G-S., Peng, D., 2000. Weighted ENO schemes for Hamilton–Jacobi equations. SIAM J. Sci. Comput. 21 (6), 2126–2143.

Kawamura, T., Kodama, Y., 2002. Numerical simulation method to resolve interactions between bubbles and turbulence. Int. J. Heat Fluid Flow 23, 627–638.

Komori, S., Nagaosa, R., Murakami, Y., Chiba, S., Ishii, K., Kuwahara, K., 1993. Direct numerical simulation of three-dimensional open-channel flow with zero-shear gas–liquid interface. Phys. Fluids A 5, 115–125.

Labourasse, E., Lacanette, D., Toutant, A., Lubin, P., Vincent, S., Lebaigue, O., Caltagirone, J.P., Sagaut, P., 2007. Towards large eddy simulation of isothermal two-phase flows: governing equations and a priori tests. Int. J. Multiface Flow 33, 1–39.

Lakehal, D., Reboux, S., Liovic, P., 2005. SGS modelling for the LES of interfacial gas–liquid flows. La Houille Blanche – Rev. Int. L'eau 6, 125–131.

Lam, K., Banerjee, S., 1988. Investigation of turbulent flow bounded by a wall and a free surface. In: Michaelides, E.E., Sharma, M.P. (Eds.), Fundamentals of Gas–Liquid Flows, vol. 72. Springer, New York, pp. 29–38.

Lam, K., Banerjee, S., 1992. On the condition of streaks formation in a bounded turbulent flow. Phys. Fluids A 4, 306–320.

Lamb, H., 1932. Hydrodynamics. Dover Publications.

Liovic, P., Lakehal, D., 2007a. Interface–turbulence interactions in large-scale bubbling processes. Int. J. Heat Fluid Flow 28, 127–144.

Liovic, P., Lakehal, D., 2007b. Multi-physics treatment in the vicinity of arbitrarily deformable gas–liquid interfaces. J. Comput. Phys. 222, 504–535.

Lombardi, P., De Angelis, V., Banerjee, S., 1996. Direct numerical simulation of near-interface turbulence in coupled gas–liquid flow. Phys. Fluids 8, 1643–1665.

Mansour, N.N., Wray, A.A., 1994. Decay of isotropic turbulence at low Reynolds number. Phys. Fluids 6 (2), 808–814.

Mills, R.R., Kistler, A.L.J., O'Brien, V., Corrsin, S., 1958. Turbulence and Temperature Fluctuation Behind a Heated Grid. Technical Report, NACA.

Osher, S., Sethian, J., 1988. Fronts propagating with curvature dependant speed: algorithms based on Hamilton–Jacobi formulations. J. Comput. Phys. 79, 12–49.

Perot, B., Moin, P., 1995. Shear-free turbulent boundary layers. Part 1. Physical insights into near-wall turbulence. J. Fluid Mech. 295, 199–227.

Pope, S.B., 2000. Turbulent Flows. Cambridge University Press.

Rogallo, R.S., 1981. Numerical Experiments in Homogeneous Turbulence. Technical Report TM 81315, NASA.

Scardovelli, R., Zaleski, S., 1999. Direct numerical simulation of free surface and interfacial flow. Annu. Rev. Fluid Mech. 31, 567–603.

Serra, J., 1983. Image Analysis and Mathematical Morphology. Academic Press, Inc., Orlando, FL, USA.

Shu, C.-W., 1997. Essentially Non-oscillatory and Weighted Essentially Non-oscillatory Schemes for Hyperbolic Conservation Laws. Technical Report, ICASE – NASA Report.

Smith, LM., Reynolds, W.C., 1992. On the Yakhot–Orszag renormalization group method for deriving turbulence statistics and models. Phys. Fluids 4, 364–390.

Sussman, M., Smereka, P., Osher, S., 1994. A level set approach for computing solutions to incompressible two-phase flow. J. Comput. Phys. 114, 146–159.

Tatebe, O., 1996. MGCG Method, A Robust and Highly Parallel Iterative Method. PhD Thesis, University of Tokyo.

Temam, R., 1969. Sur l'approximation de la solution des équations de Naviers–Stokes par la méthode des pas fractionnaires. Arch. Rat. Mech. Anal. 33, 377–385.

Toutant, A., Fournier, C., Chandesris, M., Jamet, D., Lebaigue, O., 2007. Interfacial conditions at a filtered interface for les two-phase flows. In: ICMF 2007, Germany.

Trontin, P., Vincent, S., Estivalezes, J.L., Caltagirone, J.P., 2008. Detailed comparisons of front-capturing methods for turbulent two-phase flows simulations. Int. J. Numer. Methods Fluids 56 (8), 1543–1549.

Trottenberg, U., Schuller, A., 2001. Multigrid. Academic Press, Inc..

Vincent, S., Larocque, J., Lacanette, D., toutant, A., Lubin, P., Sagaut, P., 2008. Numerical simulations of phase separation and a priori two-phase LES filtering. Comput. Fluids 37 (7), 898–906.

Walker, D.T., Leighton, R.I., Garza-Rios, L.O., 1996. Shear-free turbulence near a flat free surface. J. Fluid Mech. 320, 19–51.

Yeung, P.K., Pope, S.B., 1988. An algorithm for tracking fluid particles in numerical simulations of homogeneous turbulence. J. Comput. Phys. 79, 373–416.

Yu, H., Girimaji, S.S., Luo, L.S., 2005. Latice Boltzmann simulations of decaying homogeneous isotropic turbulence. Phys. Rev. E 71, 016708.